

## RESEARCH ARTICLES

# Trade-off between seismic source detail and crustal heterogeneities in spherical 3D finite element modeling: a 2004 Sumatra earthquake case study

Manuela Volpe<sup>1,\*</sup>, Daniele Melini<sup>1</sup>, Antonio Piersanti<sup>1</sup>

<sup>1</sup> Istituto Nazionale di Geofisica e Vulcanologia – INGV, Sezione Roma 1, Rome, Italy

## Article history

Received March 3, 2010; accepted December 22, 2010.

## Subject classification:

Finite-element method, 3D modeling, Static deformation, Sumatra earthquake.

## ABSTRACT

Finite-element methods are a powerful numerical simulation tool for modeling seismic events, as they allow three-dimensional complex models to be solved. We used a three-dimensional finite-element approach to evaluate the co-seismic displacement field produced by the devastating 2004 Sumatra–Andaman earthquake, which caused permanent deformations that were recorded by continuously operating GPS networks in a region of unprecedented area. Previous analysis of the static displacement fields have focused on the heterogeneous distribution of moment release on the fault plane; our intention here is to investigate how much the presence of crustal heterogeneities trades-off seismic source details. To achieve this aim, we adopted a quite simple source model in modeling the event. The key feature of our analysis is the generation of a complex three-dimensional spherical domain. Moreover, we also carried out an accurate analysis concerning the boundary conditions, which are crucial for finite-element simulations.

## 1. Introduction

Three-dimensional (3D) finite-element (FE) earthquake simulation is an excellent tool to investigate tectonic deformation, since it allows accurate modeling of geometrically complex domains, complicated faulting systems, and heterogeneous material property distributions. Indeed, FE modeling can be considered one of the most versatile and accurate numerical methods to solve geophysical problems, even though it is computationally demanding and intrinsically limited to manage finite domains. This last point requires the boundary conditions (BCs) to be taken care of, which still represent an open problem in FE methods.

This study is based on 3D FE earthquake modeling. We present a methodological study aimed at (i) addressing the effects of geometrical and rheological complexities on a model-predicted earthquake displacement field on a large scale; and (ii) demonstrating the trade-off between seismic source details and crustal heterogeneities. We also analyze the impact

of numerical artifacts that can be introduced by BCs. We used the 2004 Sumatra–Andaman earthquake as a case study.

The Sumatra event was one of the largest megathrust events of the last century, and it originated from complex slip on the fault along the subduction zone where the oceanic portion of the Indian Plate slides under the Eurasian Plate. Using different datasets and techniques, the magnitude of the event was estimated to be within a range of values between  $M_w = 9.0$  and  $M_w = 9.3$  [Ammon et al. 2005, Banerjee et al. 2005, Park et al. 2005, Stein and Okal 2005, Vallée 2007], depending on assumptions about the fault geometry and the amount of aseismic slip included in the source model. The slip distribution was estimated from seismic waves [Ammon et al. 2005, Lay et al. 2005], static offsets [Banerjee et al. 2005, Vigny et al. 2005, Boschi et al. 2006, Subarya et al. 2006], remote-sensing measurements [Meltzner et al. 2006, Subarya et al. 2006, Tobita et al. 2006], and joint seismic–geodetic data [Chlieh et al. 2007]. The overall magnitude of the earthquake was further constrained by the free oscillations of the Earth [Park et al. 2005, Stein and Okal 2005]. Some moderate far-field analyses of GPS data, based on laterally homogeneous numerical modeling, explain particular features of the quasi-static deformation field detected, in terms of small-scale complexities of the slip distribution on the faulting plane [Banerjee et al. 2005, Boschi et al. 2006].

On the contrary, we adopted a quite simple source model, based on five centroid–moment–tensor (CMT) point sources according to Tsai et al. [2005], to study the effects of 3D features, such as sphericity and lateral rheological heterogeneities, on the deformation field produced by the earthquake. To achieve this aim, we used a recently developed FE simulation tool, FEMSA, which is the acronym for «FE modeling for seismic applications» [Volpe et al. 2007]. FEMSA is based on CalculiX, a free 3D FE software distributed under the terms of the GNU General Public License (see <http://www.calculix.de>). In addition, we

exploited the capabilities of an external mesher, Cubit, from Sandia National Laboratories (see <http://cubit.sandia.org>), a full-featured software tool-kit for geometry preparation and robust generation of 2D and 3D FE meshes. We used Cubit to build up a complex and realistic spherical model, marked by 3D meshing with rheological layering and lateral variations of the rheological properties.

This paper is organized as follows: in Section 2 we briefly review the computational method; in Section 3 we describe the FE model of the area investigated; in Section 4 we discuss our results; and our concluding remarks are summarized in Section 5.

## 2. Computational details

We recently developed a flexible, versatile and robust numerical simulation tool (FEMSA) to investigate crustal deformation produced by arbitrary seismic dislocations by means of the FE method [Volpe et al. 2007]. FEMSA is basically a package composed of interface codes designed to automatically embed faulting sources in plane or spherical domains and to set up and run the simulation. The FE analysis is carried out by the CalculiX solver (see <http://www.calculix.de>), a freely distributed 3D structural-analysis software.

Dislocations in FE modeling are commonly treated by contact or split-node techniques. In the first case, contact interfaces between deformable bodies with stick and finite frictional slip are introduced [Xing and Makinouchi 2000, Xing and Makinouchi 2002, Cianetti et al. 2005]; in the second case, special nodes shared by two elements are defined at which the displacement depends upon which element it is referred to [Melosh and Raefsky 1981]. Different from these approaches, in our simulations we apply the equivalent body force theorem by incorporating seismic sources as appropriate distributions of double couples of forces [Burridge and Knopoff 1964, Dahlen 1972]. The reason is that CalculiX does not currently allow any of the two mentioned techniques: indeed, contact capabilities are limited to frictionless contact, which turns out not to be suitable to simulate faulting (except for tensile openings), and nodes at the element interface are not splittable.

Actually, FEMSA generates the seismic source as a 0D, 1D or 2D distribution of double couples, by defining the force field to be applied to suitably selected nodes, according to the fault geometry and the total seismic moment  $M_0$ . The rake angle  $\lambda$  is taken into account by handling oblique slip as a superposition of a pure strike and a pure dip slip mechanism, each having seismic moment  $M_s = M_0 |\cos \lambda|$  and  $M_d = M_0 |\sin \lambda|$ , respectively. An almost arbitrary fault geometry can be handled, consistent with the mesh resolution. Depending on the rheology of the domain, the source generation algorithm manages the strike and dip angles differently in defining the fault orientation. For

laterally homogeneous domains, the dip angle is fixed during the source generation stage, while, owing to the symmetry properties of the system, arbitrary strike angles are addressed by means of a reference frame rotation of the displacement field produced by the zero-strike fault. This strategy, when applicable, leads to consistent time savings, especially when a large number of models needs to be computed, for instance when solving an inverse problem; however, it cannot be applied if lateral heterogeneities are involved. In such a case, both the strike and the dip angles are considered in setting the fault geometry.

In practice, nodes in groups of four, corresponding to force application points, are suitably picked from the mesh according to the slip vector and, if needed, moved to match the correct orientation, depending on the fault geometry. The force field is then defined by computing the Cartesian components of the forces for each selected node.

A special remark is dedicated to BCs, as the FE method is limited to manage finite domains. In the literature, BCs are commonly established by imposing null displacements at the domain boundaries [Megna et al. 2005, Masterlark and Hughes 2008] or by keeping nodes on the bottom and lateral surfaces fixed in the direction perpendicular to the surface itself [Cianetti et al. 2005]. In a previous study [Volpe et al. 2007], we carried out an optimization of BCs, resulting in the occurrence of pronounced artificial effects as we approach the edges, when the cited BCs were applied. A better, although still not optimal, solution is achieved with inhomogeneous boundary conditions, by analytically computing the expected displacements at nodes on the bottom and lateral edges. We used the Okada analytical solutions [Okada 1985, 1992], which allows the investigation of crustal deformation within an isotropic elastic half-space, as a reference model. This approach is formally correct only as long as rheologically homogeneous plane domains are used, while it represents an approximation if rheological heterogeneities and/or a spherical geometry are introduced, as in the present case. This issue will be more thoroughly discussed in Section 4.

It is worth stressing that BCs are a crucial point in FE simulations, especially when complex domains are involved. The main shortcoming is that any condition applied to a finite 3D domain introduces a non-physical constraint that may shadow the effect of the heterogeneities. A possible solution would be provided by infinite elements, which are commonly derived from standard finite elements by modifying the shape functions, and which are used to extend the FE method to unbounded domain problems [Bettes 1992, Dong and Selvadurai 2009]. Nevertheless, such an approach does not represent the best solution for our purposes, as it approximates an infinite medium, while the peculiarity of the spherical approach is just the finiteness of the domain. The alternative that definitely would allow the

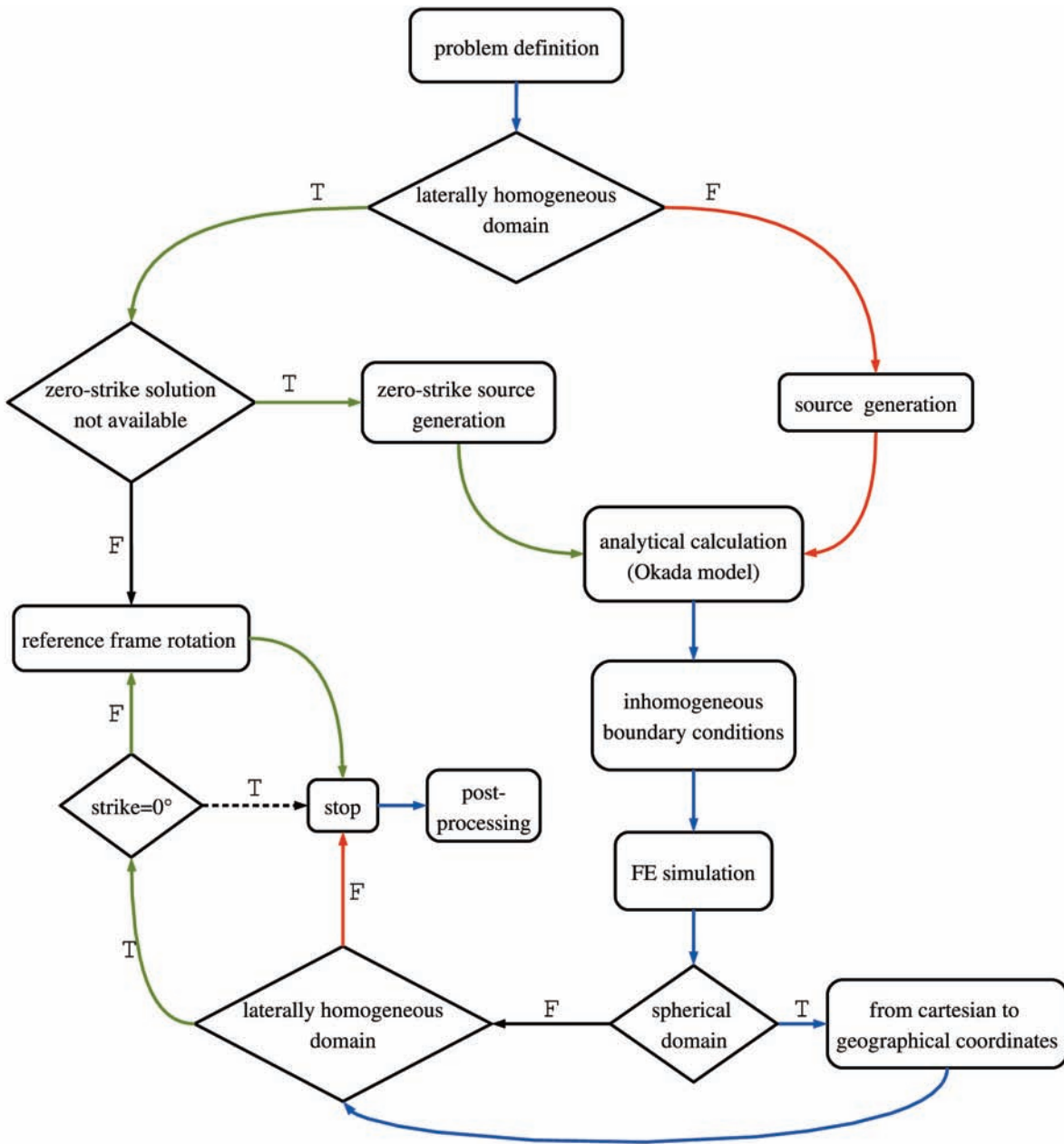


**Figure 1.** Block diagram of the automatic simulation procedure implemented in FEMSA, as described in the text. The green path is related to laterally homogeneous domains, the red path is related to domains with lateral variations of the rheological properties, while the blue path is shared between the two types of domain.

problem to be bypassed is to simulate a self-gravitating sphere representing the entire Earth. This poses many theoretical and computational challenges and will be the goal of our future work.

The FEMSA package is built-up to operate in an automatic way. In Figure 1, a schematic block diagram of the simulation procedure is shown: (i) the seismic source is generated; (ii) the displacement field is analytically calculated according to the Okada model; (iii) the inhomogeneous BCs are formulated and formalized, as explained above; (iv) the FE simulation is carried out; (v) the reference frame transformation is applied to the numerical solution to account for model sphericity; and (vi) in the case of a laterally homogeneous domain, reference-frame rotation is

applied to the numerical solution to account for an arbitrary strike angle. Note that the geometry and mesh definition do not appear in the diagram, since they represent an independent pre-processing step for the simulation.

### 3. The simulation model

Due to the unusual size of the event, the investigation of the crustal deformation produced by the Sumatra earthquake requires a very-long-range analysis, where curvature effects cannot be neglected. In a previous study [Volpe et al. 2007], we described a first preliminary approach based on a relatively rough 3D model (hereinafter referred to as the V07 model), generated through the native CalculiX pre-processor (cgx), an interactive 3D graphical interface. In

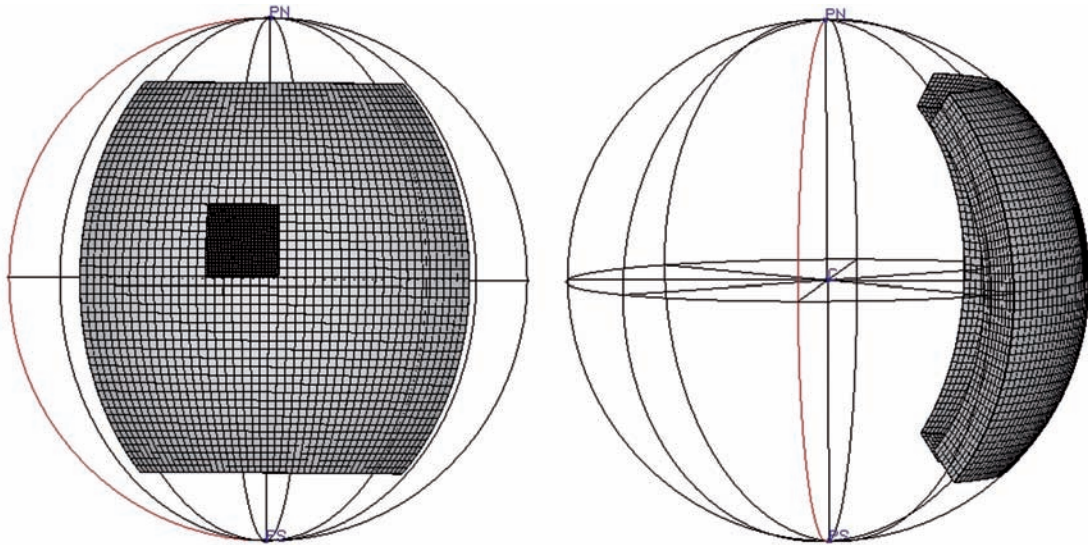


**Figure 2.** Front and lateral views of the mesh generated by cgx [Volpe et al. 2007]. The wire-framed sphere is only displayed for presentation purposes.

the present study, in order to improve that model and better account for detailed features, we built-up a more complex and realistic model (hereinafter referred to as the C01 model) by means of the Cubit mesher. The advantages in using Cubit over the native CalculiX mesher are the stronger automation in both the geometry and mesh generation process, the ability of achieving unstructured complex meshes, and the better control over the mesh density and quality.

Both the V07 and C01 models are 3D spherical domains, consisting of a portion of a spherical zone about 1000 km thick and discretized using 20-node brick elements. The mesh density is controlled by generating a finer mesh near the seismic source, where high stress and strain gradients are expected, and a coarser mesh in areas of reasonably constant stress, in order to achieve the best trade-off between accuracy of the solution and computational cost of the analysis. We assumed multi-layered elastic domains to

investigate the co-seismic deformation field by means of a static calculation.

In the V07 model [Volpe et al. 2007], the domain spans about  $9 \times 10^7 \text{ km}^2$  on the Earth surface. A FE structured mesh was generated, made by 38,348 elements, resulting in 171,537 nodes. The element size is about 40 km near the source and about 200 km outside of the source region. The model is shown in Figure 2. The rheological parameters were obtained from the volume-averaged values of the Lamé constants according to the Preliminary Reference Earth Model (PREM) [Dziewonski and Anderson 1981].

In the C01 model, the domain spans about  $1.2 \times 10^8 \text{ km}^2$  on the Earth surface. We introduced a realistic rheological contrast between the continental and oceanic lithospheres, by (conservatively) extracting the  $-500 \text{ m}$  interface from a global seafloor topography model, to retrieve the continental margins. The geometrical model is displayed in Figure 3. The

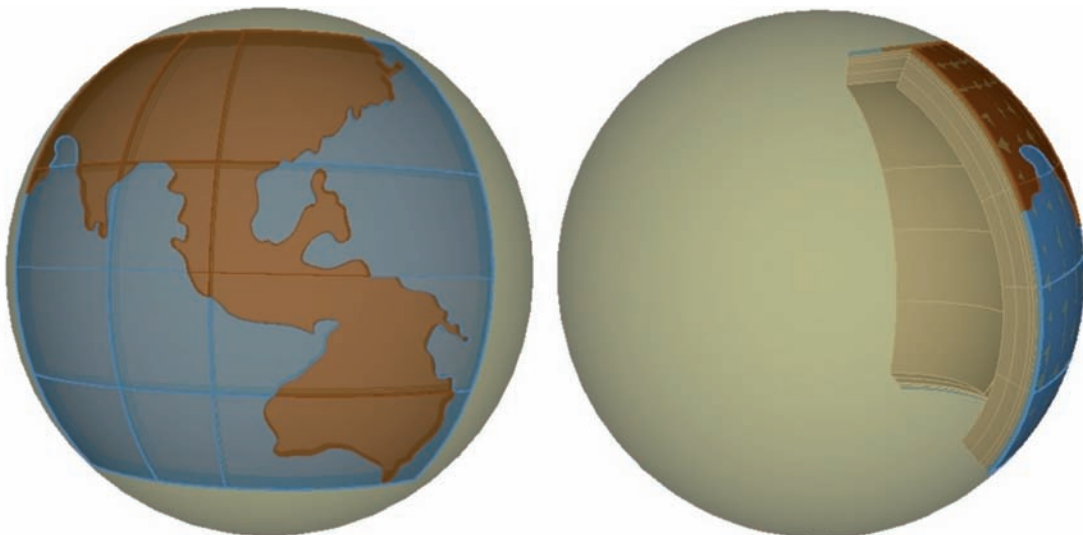


**Figure 3.** Pictorial view of the model generated by Cubit. A front and a lateral perspective of the domain are shown, both being represented on the sphere for a better view. The contrast between the continental and the oceanic lithospheres is emphasized by color.

domain was discretized, generating an unstructured mesh with 189,184 elements, resulting in 800,114 nodes. The element size is biased from 20 to 400 km using the paving meshing algorithm in combination with an appropriate adaptive sizing function. A front view of the mesh is shown in Figure 4. The contrast between the continental and oceanic lithospheres was introduced for a thickness of 40 km from the surface, which are composed of four 10-km-thick layers, with rheological parameters for each layer deduced from the depth profiles of the seismic velocities and densities provided by Mooney et al. [1998]. At depths greater than 40 km, the domain is split into laterally homogeneous layers with variable thicknesses, the elastic constants of which are calculated from the *ak135* velocity model proposed by Kennen et al. [1995].

The seismic source has been modeled with the multiple CMT solution proposed by Tsai et al. [2005], which consists of five point sources, fitting mantle-wave data registered in the 200–500 s period range by the Incorporated Research Institutions for Seismology (IRIS) Global Seismographic Network. All centroid depths are fixed at 25 km. Such a model results in a total seismic moment of  $1.17 \times 10^{23}$  N·m, equivalent to a moment magnitude  $M_w = 9.3$ . Three large slip patches (27%, 33% and 24% of the total moment) are located in the southern region of the fault, while the moment releases further north represent about 9% and 7% of the total. The focal mechanisms of the five sources change systematically from south to north: the strike rotates clockwise and the slip vectors rotate from nearly pure thrust to oblique slip with a large right-lateral strike slip component. In our simulations, the analysis with multiple sources is actually treated as a superposition of multiple single sources. We note that the roughness of the adopted

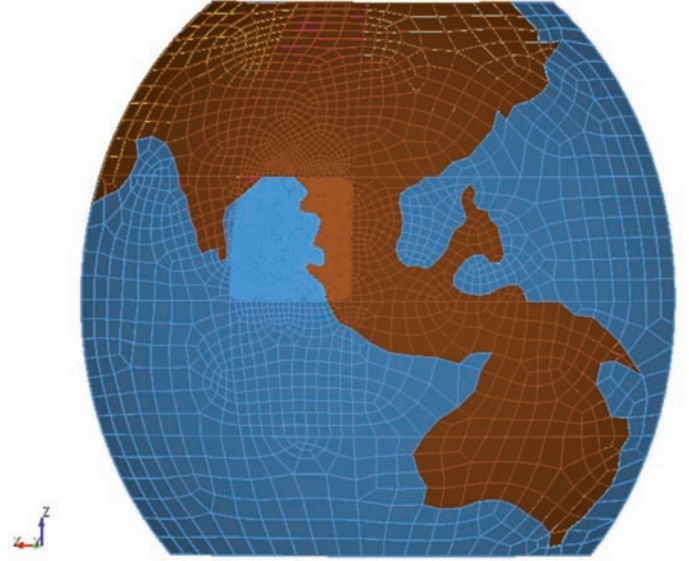


Figure 4. Front view of the unstructured mesh generated by Cubit.

source model is intentional, in order to indicate the trade-off with the real 3D features of the simulation domain.

#### 4. Results and discussion

The models described in the previous section were solved to obtain the co-seismic deformation field produced by the 2004 Sumatra earthquake, and the synthetic displacements were compared with a subset of geodetic measurements recorded by continuously operating GPS networks. During the analysis, the rheology was modified, generating a set of FE models as summarized in Table 1.

Also, different BCs were examined using the Okada analytical solution, as described above. Neglecting both curvature and lateral heterogeneities, such an approximation introduces a bias into the simulation results and influences

Model	Geometry	Mesher	Rheology	Lateral heterogeneities	BC	Rigidity softening
V07	spherical	cgx	layered	no	averaged <sup>a</sup>	no
P01	planar	Cubit	homogeneous <sup>d</sup>	no	averaged <sup>a</sup>	no
C01	spherical	Cubit	layered	yes	averaged <sup>a</sup>	no
C02	spherical	Cubit	layered	yes	layered <sup>b</sup>	no
C03	spherical	Cubit	layered	yes	layered <sup>b</sup>	yes <sup>e</sup>
C04	spherical	Cubit	layered	yes	layered <sup>b</sup>	yes <sup>f</sup>
C05	spherical	Cubit	layered	yes	averaged <sup>c</sup>	yes <sup>f</sup>
C06	spherical	Cubit	homogeneous <sup>d</sup>	no	averaged <sup>a</sup>	no
C07	spherical	Cubit	homogeneous <sup>d</sup>	no	averaged <sup>d</sup>	yes <sup>g</sup>
C08	spherical	Cubit	homogeneous <sup>d</sup>	no	averaged <sup>a</sup>	yes <sup>h</sup>

**Table 1.** Summary of the characteristics of the FE models implemented in the present study. <sup>a</sup>: the total volume-averaged PREM rigidity value is used; <sup>b</sup>: the layer-by-layer rigidity values are used; <sup>c</sup>: the first 10-km-thick layer rigidity value is used; <sup>d</sup>: the reduced total volume-averaged PREM rigidity value is used; <sup>e</sup>: applied in the source region in the depth range 10–40 km; <sup>f</sup>: applied in the source region in the depth range 0–100 km; <sup>g</sup>: applied in the whole domain; <sup>h</sup>: applied in the whole domain except the edges.

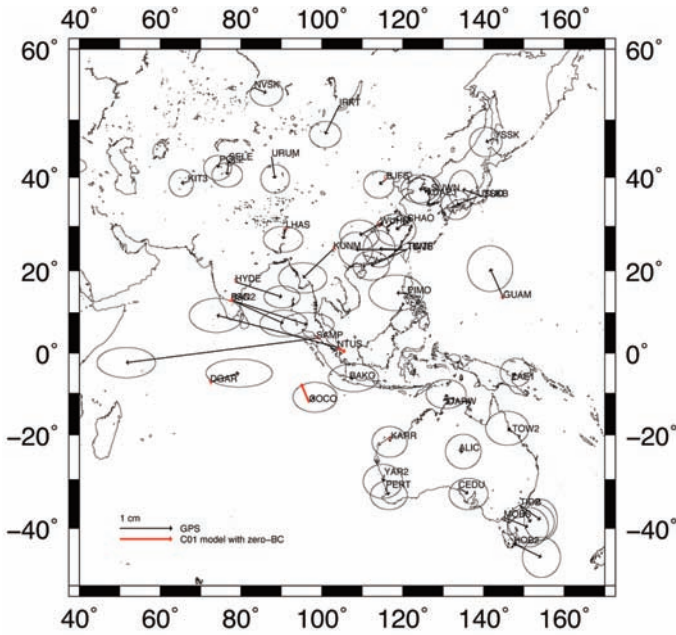


**Figure 5.** Comparison between GPS measurements from Boschi et al. [2006] and the horizontal displacements resulting from the FE simulations on the C01 model with zero displacement along the boundaries. Error ellipses correspond to 90% confidence.

the fit of the data, when it is assigned to a heterogeneous spherical domain. Nevertheless, the goal of the present study is not to provide an improvement to the modeling of the Sumatra static deformation with respect to published studies (e.g. Chlieh et al. 2007), but to investigate the role of rheological complexities and the trade-off with the source details. In any case, we considered that our BC approximation is a good alternative with respect to the hypothesis of zero displacement along the boundaries, which in this case turns out to dump the deformation and would require a larger model size (Figure 5).

We should note that in the very far-field, the recorded offsets are not fitted by our calculations; a similar effect has been detected with other approaches [Banerjee et al. 2005, Boschi et al. 2006], where, moreover, deformations appear overestimated. Indeed, modeling is affected by edge effects at a long distance from the source, due to the proximity of the mesh boundaries. In addition, the GPS offsets registered

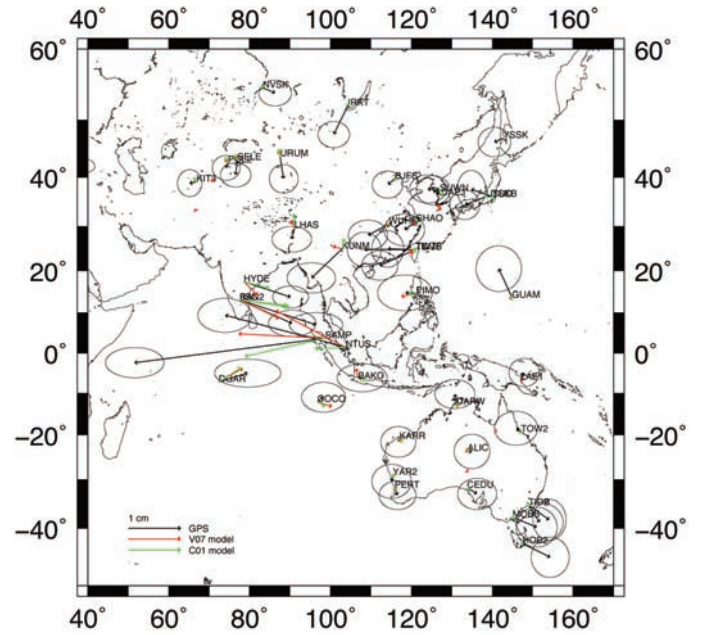


**Figure 6.** Comparison between GPS measurements from Boschi et al. [2006] and the horizontal displacements resulting from the FE simulations on the V07 and C01 models. Error ellipses correspond to 90% confidence.

in these regions cannot be unambiguously associated with the earthquake, as the occurrence of spurious signals cannot be excluded.

Instead, we focused our attention on the moderate far-field (Indian Ocean area) and the Indian region, where other numerical analyses neglecting lateral variations of the rheological properties [Banerjee et al. 2005, Boschi et al. 2006] can fit the measured displacements only by introducing strong constraints on the source model, in the form of a highly heterogeneous slip distribution. In these zones, we are able to acceptably fit GPS measurements from the dataset obtained by Boschi et al. [2006], holding to the well-known limits of our modeling.

As a first step, inhomogeneous averaged BCs were applied, by computing the Okada displacements at the boundary nodes using the elastic parameters calculated from the total volume averaged PREM values of the Lamé constants, neglecting rheological layering. In Figure 6, the

	GPS	V07	C01	C02	C03	C04
SAMP	14.62 ± 4%	6.64 (−55%, 46.8)	6.27 (−57%, 35.9)	6.33 (−57%, 34.3)	6.63 (−55%, 31.9)	8.71 (−40%, 23.4)
NTUS	2.32 ± 22%	1.50 (−37%, 4.6)	0.58 (−75%, 11.3)	0.54 (−77%, 12.1)	0.55 (−77%, 12.0)	0.60 (−75%, 12.3)
HYDE	0.94 ± 38%	0.37 (−61%, 4.3)	0.50 (−47%, 4.3)	0.46 (−51%, 4.1)	0.44 (−53%, 4.2)	0.46 (−51%, 4.4)
IISC	1.52 ± 34%	0.82 (−46%, 4.1)	0.95 (−38%, 5.3)	0.85 (−44%, 5.2)	0.85 (−44%, 5.1)	0.89 (−41%, 5.4)
BAN2	1.10 ± 43%	/	0.90 (−17%, 3.4)	0.81 (−26%, 3.5)	0.81 (−26%, 3.4)	0.85 (−22%, 3.6)

**Table 2.** Absolute value of the horizontal displacement vector on a set of GPS sites from the dataset of Boschi et al. [2006] and from FE simulations. The vector magnitude is expressed in cm. The relative error, defined as  $(|u_{FE}^E| - |u_{GPS}^E|) / |u_{GPS}^E| \times 100$ , and the misfit, defined as  $(|(u_{FE}^E - u_{GPS}^E) / \sigma_{GPS}^E| + |(u_{FE}^N - u_{GPS}^N) / \sigma_{GPS}^N|)$ , are also indicated in the brackets.

synthetic displacements calculated from the V07 and C01 models are compared with the GPS data from Boschi et al. [2006]. It is worth noting that in the V07 model, GPS sites are often not coincident with mesh nodes, due to the poor resolution, and the displacement on the closest node is considered in the comparison. On the contrary, the finer mesh of the C01 model allows a more precise comparison with the GPS data. In Table 2, the modeled vector magnitude on the sites inspected, their relative error, and the misfit with respect to the experimental measurements are compared.

At GPS sites located in the Indian Ocean area, the data fit is acceptable if the roughness of the seismic source model is taken into account. In particular, at the nearest stations (SAMP and NTUS), which are the most sensitive to the detailed source structure, the direction of the modeled vectors is in satisfactory agreement with the observations, while their magnitude is relatively underestimated. At the SAMP site, the C01 model improves the agreement, while at the NTUS station, the V07 model better reproduces the observed offset both in direction and (especially) in magnitude. More importantly, we note that although the displacements are again underestimated, there is relatively good agreement at the Indian sites (HYDE, IISC and BAN2), which Banerjee et al. [2005] and Boschi et al. [2006] managed to fit with a laterally homogeneous model only at the cost of introducing a large number of free parameters associated with a highly heterogeneous distribution of slip in the source model, which is not confirmed by seismological models. We stress that the poor spatial resolution of the V07 model does not allow it to discern between the BAN2 and the IISC stations, due to their small relative distance, while the C01 model does. The vector orientation at the HYDE station is better matched by the C01 model, while the opposite holds for the IISC station. We would like to note that our fit is strongly bound to the geometry of the simulation domain: a test simulation on a multi-layered laterally homogeneous plane domain (hereinafter referred to as the P01 domain), with a resolution similar to the V07 model, failed in predicting the orientation of the co-seismic displacements at the Indian stations, as is shown in Figure 7. This observation confirms that curvature has an important effect on the computed results.

The comparison between plane and spherical geometry requires a small digression concerning the moderate far-field. From Figure 7, we note that the static offset at the SAMP station is better reproduced by the P01 domain than the V07 or C01 models. A similar behavior is observed in the realm of semi-analytical spherical models, where finite faults are approximated by a superposition of point sources: in this case, a more precise estimation of moderate far-field effects is obtained with planar models, where the finite source is fully analytically implemented, since the calculation is not affected by discretization [Piersanti et al. 1997, Nostro et al. 1999]. In

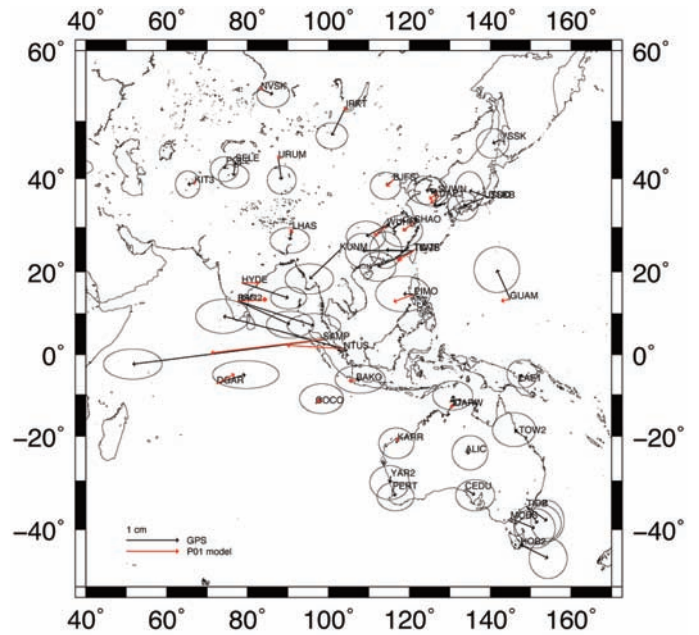


Figure 7. Comparison between GPS measurements from Boschi et al. [2006] and the horizontal displacements resulting from the FE simulation on the flat P01 domain. Error ellipses correspond to 90% confidence.

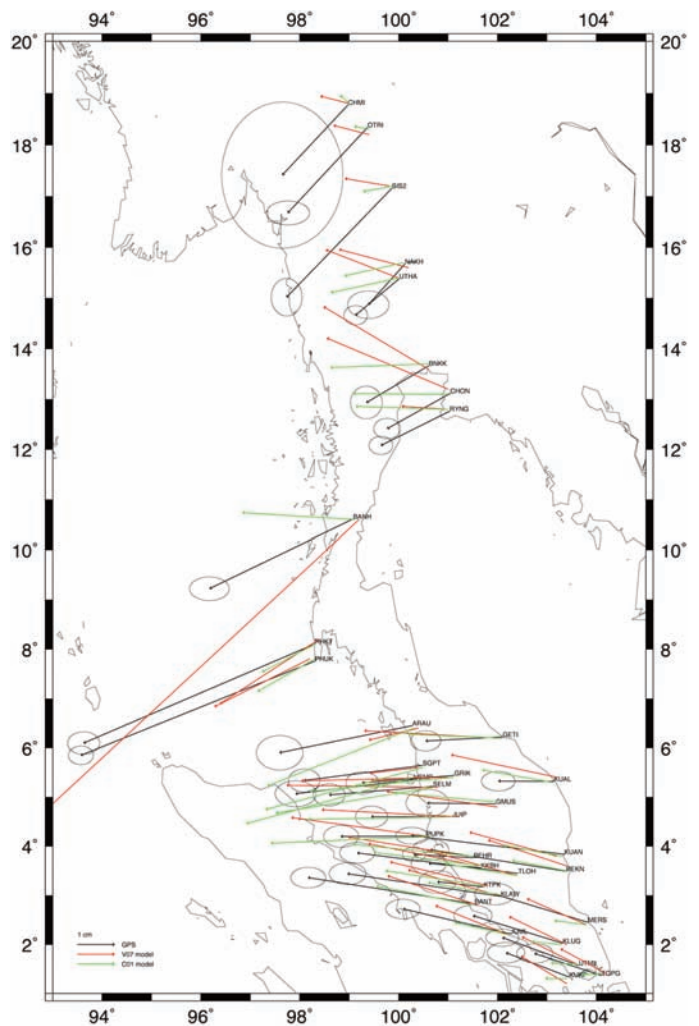
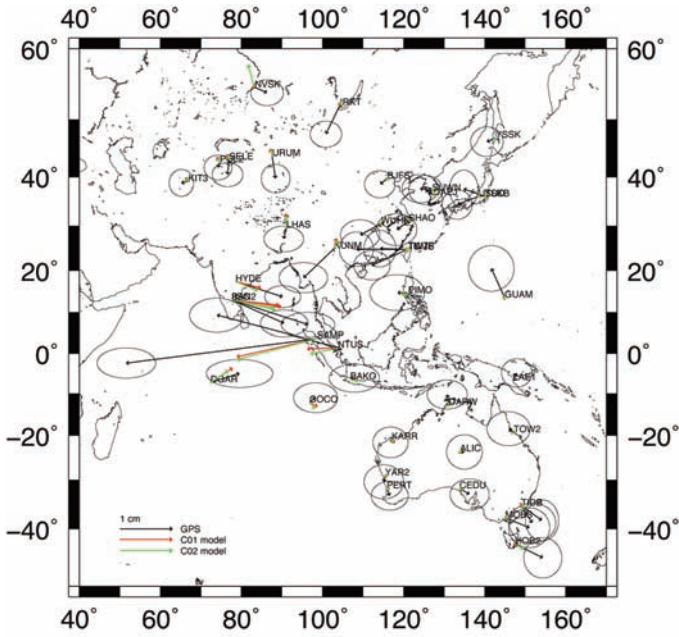
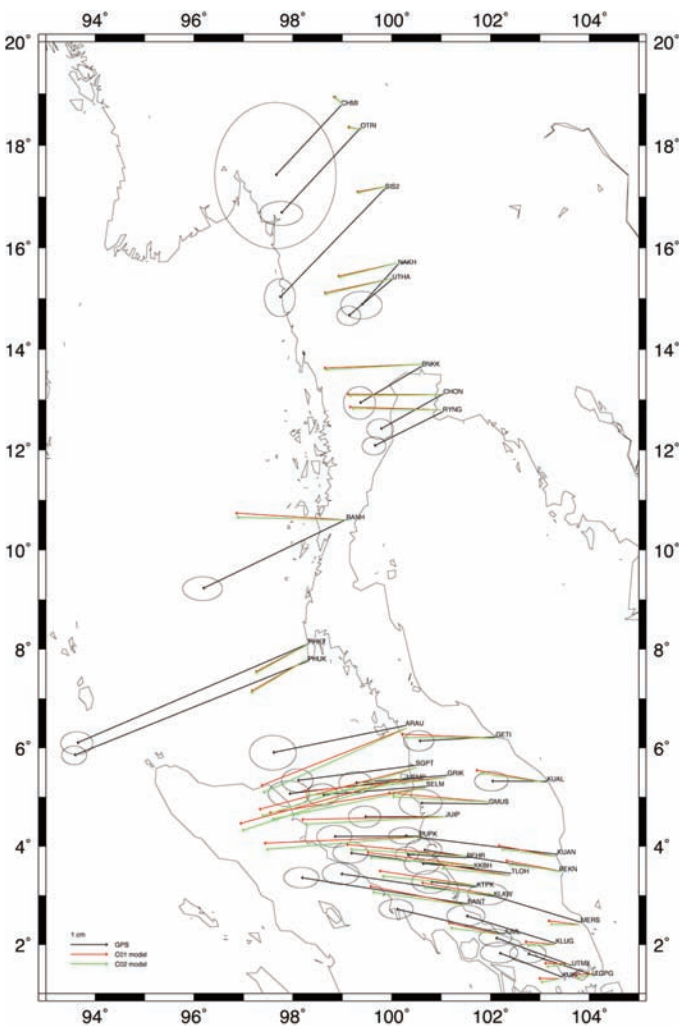


Figure 8. Comparison between GPS measurements from Vigny et al. [2005] and the horizontal displacements resulting from the FE simulations on the V07 and C01 models. Error ellipses correspond to 60% confidence.



**Figure 9.** Comparison between GPS measurements from Boschi et al. [2006] and the horizontal displacements resulting from the FE simulations on the C01 and C02 models. Error ellipses correspond to 90% confidence.



**Figure 10.** Comparison between GPS measurements from Vigny et al. [2005] and the horizontal displacements resulting from the FE simulations on the C01 and C02 models. Error ellipses correspond to 60% confidence.

our simulations, a multiple point source model is introduced in both the plane and the spherical models. Consequently, the difference in the moderate far-field results has to be accounted for as the long-range effect of the Okada BCs, which are better matched by the plane model. In this respect, the simulation on the entire sphere is confirmed as necessary.

Since the dataset of Boschi et al. [2006] is lacking in moderate far-field data, we also compared our results with GPS measurements from Vigny et al. [2005], focusing on the source region. From Figure 8, we can note that displacements computed with the C01 model are almost systematically shorter than those computed with the V07 model, with few exceptions. In some cases, this implies a better agreement with GPS offsets (for example at stations KUAL and GETI), while in other cases the fit is worse (for example at stations PHKT and PHUK). Anyway, the orientation of the vectors appears to be improved in the C01 model with respect to the V07 model.

In order to improve the simulation, we refined the BCs for the C01 model: we took into account the rheological layering and solved the Okada model for each layer using the appropriate set of elastic constants; the corresponding computed displacements are then prescribed to nodes located on the boundaries of the same layer. In the following, this will be referred to as the C02 model.

From Figure 9, where the comparison with the C01 model and GPS data is shown, and from Table 2, we infer that the upgrading from the C01 to the C02 model has very little effect on the simulation results.

Distance from the surface (km)	C01, C02		C03		C04, C05	
	cont.	oce.	cont.	oce.	cont.	oce.
0–10	0.58	0.58	0.58	0.58	0.19	0.19
10–20	3.43	6.48	0.86	1.62	1.14	2.16
20–30	4.33	6.88	1.44	2.29	1.44	2.29
30–40	6.48	6.88	2.16	2.29	2.16	2.29
40–80	6.71		6.71		2.24	
80–100	6.78		6.78		2.26	
100–120	6.78		6.78		6.78	
120–140	6.87		6.87		6.87	
140–240	7.07		7.07		7.07	
240–340	7.67		7.67		7.67	
340–670	10.9		10.9		10.9	
670–1000	17.3		17.3		17.3	

**Table 3.** Rigidity layering used to perform the FE simulations. The softening is only applied in the seismogenic zone. Up to 40 km from the surface, the continental and the oceanic lithospheres are differentiated. Numerical values are expressed in units of  $10^{10}$  Pa.

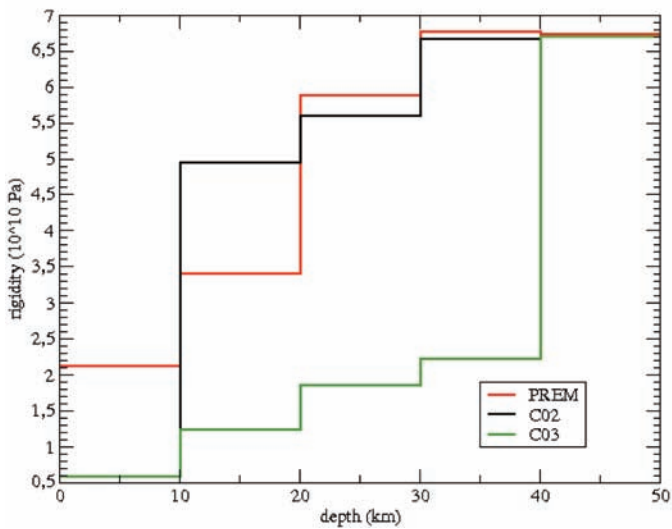


**Figure 11.** Plot of the (average) rigidity variations with depth in the range 0–50 km in the source region as fixed in the C02 (as well as C01) and C03 models, compared to the PREM values.

Ten years ago, Bilek and Lay [1999] estimated rigidity variations with depth along subduction-zone interfaces. Rigidity is a measure of the proportionality between shear stress and shear strain and it affects the degree of earthquake shaking through its influence on seismic wave speed and earthquake rupture velocity. According to their results, the average rigidity of seismogenic zones appears to increase with depth up to a factor of  $\sim 5$  in the range 5–50 km. At depths below 40 km, the estimated rigidity values are 3–4 times lower than in PREM. This result is consistent with the hypothesis that tsunami-generating earthquakes, which are typified by large slip and a slow rupture velocity, occur in regions of low rigidity at shallow depths. Several mechanisms may contribute to the trend described, but the main role appears to be played by mineralogical phase transitions within the subducting sediments and in the subducting plate, driven by the pressure and temperature increasing with depth.

We modified the rheology of the C02 model within a limited region, spanning  $4.7 \times 10^6$  km<sup>2</sup> near the source, in order to fit the rigidity trend estimated by Bilek and Lay [1999] in the seismogenic zone. Actually, this means we reduced the rigidity values in the depth range 10–40 km, as indicated in Table 3. In the following, this will be referred to as the C03 model. Figure 11 shows the average rigidity variations in the source region between depths of 0 and 50 km in the C02 and C03 models, compared to the PREM values.

In Figures 12 and 13 we compare the computed vectors and the GPS offsets from the dataset of Boschi et al. [2006] and Vigny et al. [2005], respectively. From Table 2, the Indian sites (HYDE, IISC and BAN2), which are located immediately outside the softened source region, appear not to be influenced by the softening; at the nearest stations (SAMP and

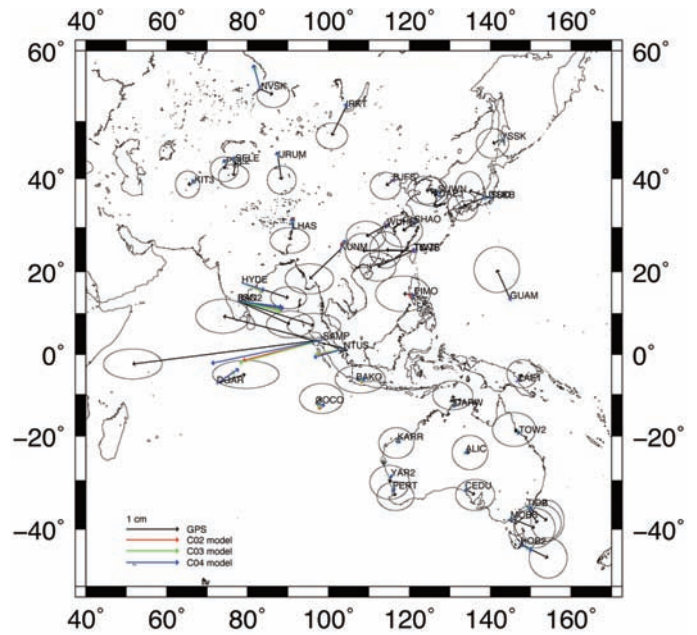


**Figure 12.** Comparison between GPS measurements from Boschi et al. [2006] and the horizontal displacements resulting from the FE simulations on the C02, C03 and C04 models. Error ellipses correspond to 90% confidence.

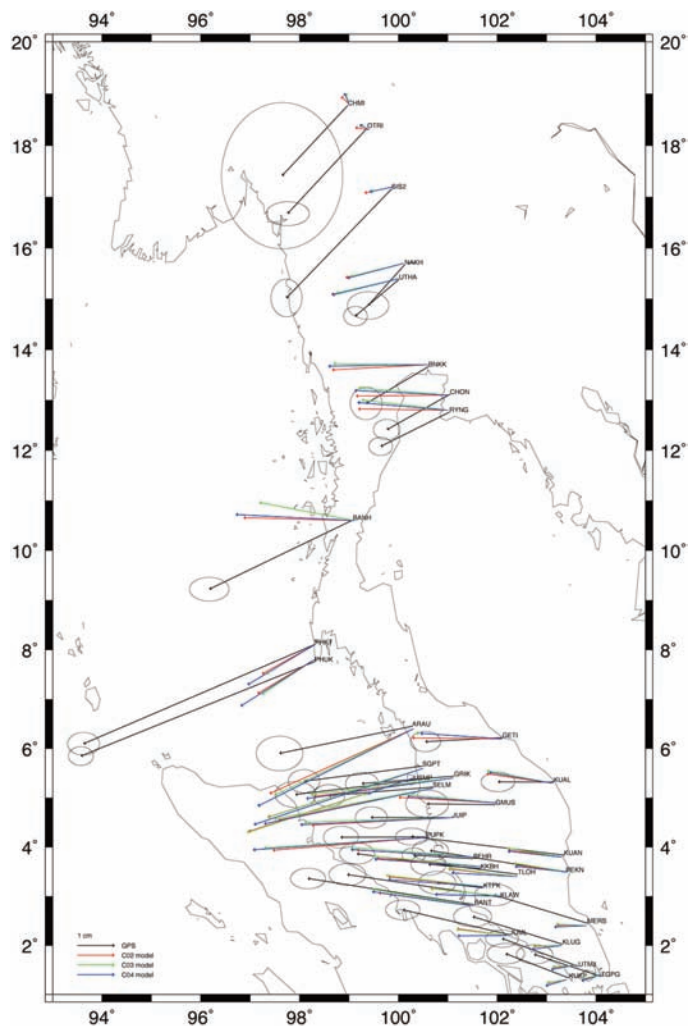


**Figure 13.** Comparison between GPS measurements from Vigny et al. [2005] and the horizontal displacements resulting from the FE simulations on the C02, C03 and C04 models. Error ellipses correspond to 60% confidence.

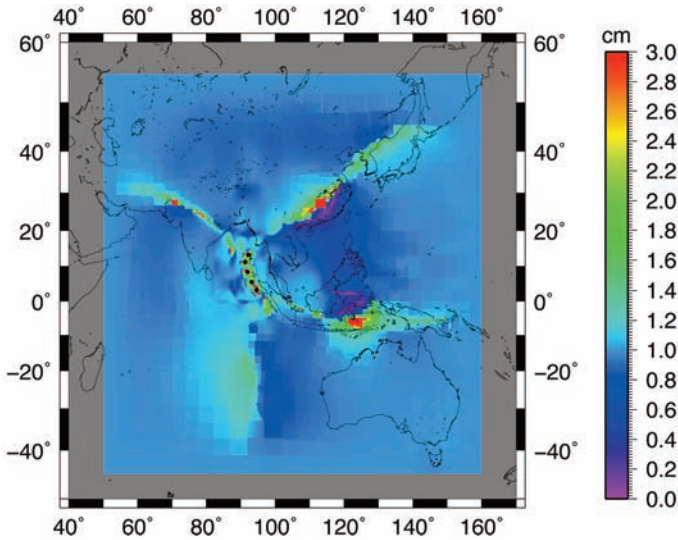


**Figure 14.** Ratio between the deformation magnitudes calculated with the C03 and C02 models.

NTUS), instead, the vector magnitude turns out to be slightly increased, but the effect is very small. Figure 14 displays the ratio between the deformation magnitude calculated with the C03 and C02 models: the rigidity reduction produces a small amplification of the displacements, which is strictly localized in the source region.

In order to inspect the behavior of our modeling by emphasizing the softening effect, we reduced the rigidity value by a factor of 3 in the depth range 0–100 km, as indicated in Table 3. In the following, this will be referred to as the C04 model. The comparison with GPS measurements and previous results from the C02 and C03 models, as

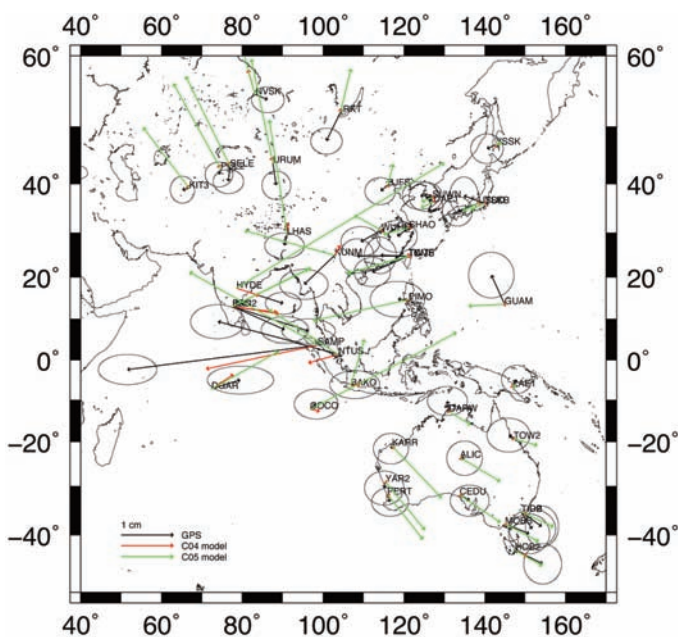


**Figure 16.** Comparison between GPS measurements from Boschi et al. [2006] and the horizontal displacements resulting from the FE simulations on the C04 and C05 models. Error ellipses correspond to 90% confidence.

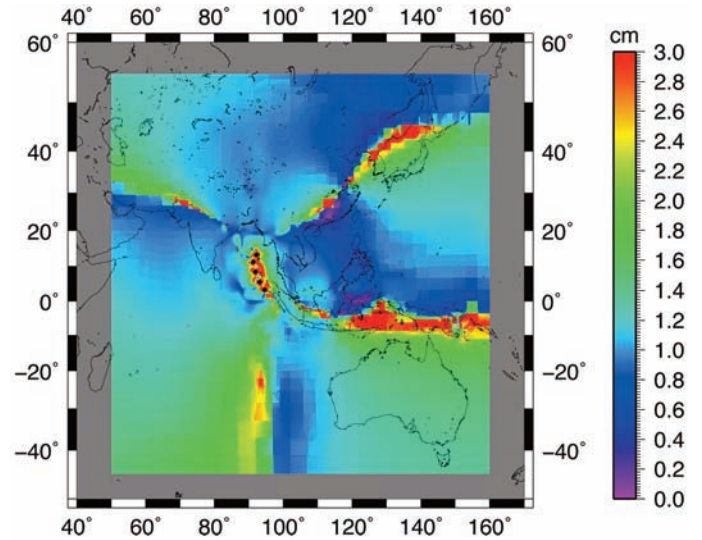


**Figure 15.** Ratio between the deformation magnitudes calculated with the C04 and C02 models.

reported in Figures 12 and 13, as well as in Table 2, shows amplification of the displacement vectors, although the magnitude of the effect is still very small. The ratio between the deformation magnitude obtained with the C04 and C02 models, shown in Figure 15, presents a larger amplification with respect to Figure 14, but is still strictly localized.

We modified the C04 model, applying averaged instead of layered BCs using the average rigidity value of the first 10-km-thick rheological layer. In the following, this will be referred to as the C05 model. The displacements obtained are compared with GPS measurements from Boschi et al. [2006] in Figure 16, and they turn out to be greatly increased in magnitude, so that now computed vectors overestimate the GPS offsets. This result is crucial, as it demonstrates that BCs heavily affect our simulations, in spite of the considerable extent of the simulation domain.

As a last check, we imposed a homogeneous rheology to the C01 model, and we adopted the composite source model derived by Tsai et al. [2005]. We first calculated crustal deformation using the elastic parameters obtained from the total volume-averaged PREM values of the Lamé constants (model C06), and then reducing the rigidity value by a factor of 3 in the whole domain, edges included (model C07). Since a linear stress–strain relationship holds within a homogeneous domain under elastic regime, the ratio between the deformation magnitudes obtained from the two models is expected to be 3 everywhere. This only occurs if the BCs are also computed with the reduced rigidity value, as shown in Figure 17. If this is not the case, i.e. if the BCs are invariably computed using the initial averaged elastic parameters of the C06 model (model C08), a very long range effect of the BCs is observed (Figure 18). This provides clear evidence that the simulation domain adopted to investigate such a great event, even if large, is not large enough to avoid edge effects also at a short distance from the source, i.e. at a large distance from

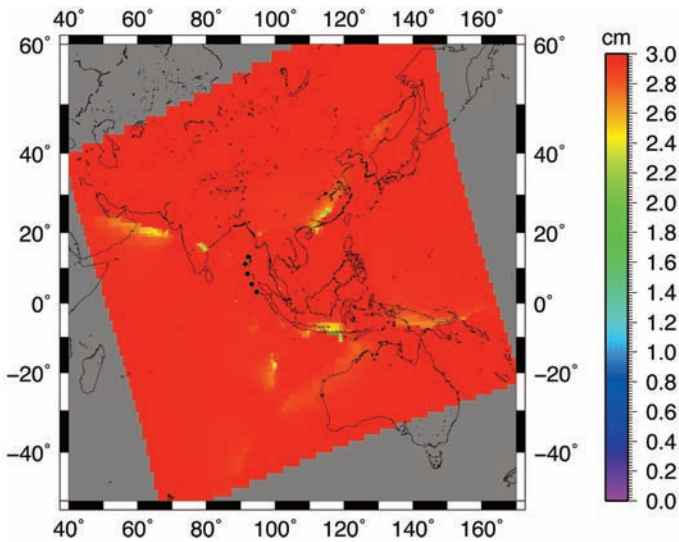


**Figure 17.** Ratio between the deformation magnitudes calculated with C07 and C06 models.

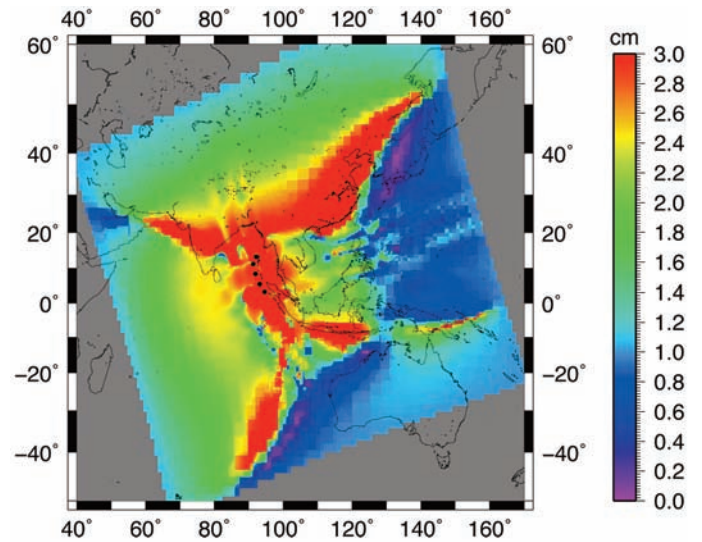


**Figure 18.** Ratio between the deformation magnitudes calculated with C08 and C06 models.

the boundaries. Future work will thus be devoted to build-up a totally spherical domain representing the entire Earth, in such a way that the BC issue will be bypassed.

## 5. Conclusions

By means of a recently developed 3D FE approach (FEMSA), we have performed a methodological study concerning the effects of 3D features, such as geometrical and/or rheological heterogeneities and BCs, on earthquake modeling. As a case study, we evaluated the co-seismic displacement field associated with the large 2004 Sumatra–Andaman earthquake. For this, we generated a complex spherical simulation domain in which a real 3D meshing was introduced as a rheological contrast between the continental and oceanic lithospheres. This was achieved by extracting the continental margins from global bathymetry data. We also took into account a realistic variation of the rheological properties with depth in the seismogenic zone, as proposed by Bilek and Lay [1999].

We compared the computed deformation field with GPS measurements using the datasets obtained by Boschi et al. [2006] and Vigny et al. [2005] and paying special attention to the moderate far-field and the Indian sites. Our results highlight the existence of a trade-off between 3D features and source details and a strong sensitivity to the BCs applied.

At present, most modeling approaches introduce a large number of free parameters to account for small-scale complexities of the slip distribution [Boschi et al. 2006, Chlieh et al. 2007] that are not necessarily connected with the physics of the event investigated. We obtained an acceptable agreement with data in the regions inspected using a simple point-source model together with a complex spherical 3D meshed simulation domain, where curvature has a crucial role. The 3D modeling partially trades-off the roughness of the source model. Of course, we do not mean that there is

no need to take into account heterogeneous energy-release mechanisms. Our point is that model complexities should be introduced with a logical and physically consistent hierarchy. The presence of major 3D geometrical and rheological features, such as sphericity or oceanic crust contrast, is certainly true, and in order to avoid artificial trade-offs, their effects should be considered before introducing further complexities, such as heterogeneous energy release on the fault plane. We note the occurrence of an asymmetry in the trade-off, since the additional parameters in our simulations are not free parameters, but real Earth complexities, which are constrained by the physical properties of the area investigated and cannot be arbitrarily tuned.

The systematic analysis of BCs revealed a very-long-range effect on the calculations, even if the simulation domain has a considerably great area. This result demonstrates that a limited domain, even if large, is not suitable to investigate the effects produced by an event of such a magnitude, requiring the generation of a self-gravitating sphere representing the entire Earth. In this respect, the Sumatra earthquake should be regarded as a real "global" event.

**Acknowledgments.** The authors are grateful to the CalculiX developers, Guido Dhondt and Klaus Wittig, and to the dedicated exchange forum for helpful discussions. The Cubit team is also thanked. Special thanks are devoted to Dr. E. Casarotti for the useful discussions. MV is supported by the MIUR-FIRB research project «Sviluppo di nuove tecnologie per la protezione e la difesa del territorio dai rischi naturali».

## References

- Ammon, C.J., C. Ji, H.-K. Thio, D. Robinson, S. Ni, V. Hjorleifsdottir, H. Kanamori, T. Lay, S. Das, D. Helmberger, G. Ichinose, J. Polet and D. Wald (2005). Rupture process of the 2004 Sumatra–Andaman earthquake, *Science*, 308, 1133-1139.
- Banerjee, P., F.F. Pollitz and R. Bürgmann (2005). Size and duration of the great 2004 Sumatra–Andaman earthquake from far-field static offsets, *Science*, 308, 1769-1772.
- Bettes, P. (1992). *Infinite Elements*, Penshaw Press, Sunderland, UK, 264 pp.
- Bilek, S.L. and T. Lay (1999). Rigidity variations with depth along interplate megathrust faults in subduction zones, *Nature*, 400, 443-446.
- Boschi, E., E. Casarotti, R. Devoti, D. Melini, A. Piersanti, G. Pietrantonio and F. Riguzzi (2006). Coseismic deformation induced by the Sumatra earthquake, *J. Geodynamics*, 42, 52-62.
- Burridge, R. and L. Knopoff (1964). Body force equivalents for seismic dislocations, *B. Seismol. Soc. Am.*, 54, 1875-1888.
- Chlieh, M., J.-P. Avouac, V. Hjorleifsdottir, T.-R.A. Song, C. Ji, K. Sieh, A. Sladen, H. Hebert, L. Prawirodirdjo, Y. Bock and J. Galetzka (2007). Coseismic Slip and Afterslip of the Great  $M_w$  9.15 Sumatra–Andaman Earthquake of 2004, *B. Seismol. Soc. Am.*, 97 (1A), S152-S173.
- Cianetti, S., C. Giunchi and M. Cocco (2005). Three-dimensional finite elements modeling of stress interaction: An application to Landers and Hector Mine fault systems, *J. Geophys. Res.*, 110, B05617; doi: 10.1029/2004JB003384.
- Dahlen, F.A. (1972). Elastic Dislocation Theory for a Self-Gravitating Elastic Configuration with an Initial Static Stress Field, *Geophys. J. R. Astr. Soc.*, 36, 461-485.
- Dong, W. and A.P.S. Selvadurai (2009). A combined finite and infinite element approach for modeling spherically symmetric transient subsurface flow, *Computers & Geosciences*, 35, 438-445.
- Dziewonski, A.M and D.L. Anderson (1981). Preliminary reference Earth model, *Phys. Earth Planet. Inter.*, 25, 297-356.
- Kennet, B.L., E.R. Engdahl and R. Buland (1995). Constraints on seismic velocities in the Earth from traveltimes, *Geophys. J. Int.*, 122, 108-124.
- Lay, T., H. Kanamori, C.J. Ammon, M. Nettles, S.N. Ward, R.C. Aster, S.L. Beck, S.L. Bilek, M.R. Brudzinski, R. Butler, H.R. DeShon, G. Ekström, K. Satake and S. Sipkin (2005). The Great Sumatra–Andaman Earthquake of 26 December 2004, *Science*, 308, 1127-1133.
- Masterlark, T. and K.L.H. Hughes. (2008). Next generation of deformation models for the 2004 M9 Sumatra–Andaman earthquake, *Geophys. Res. Lett.*, 35, L19310.
- Megna, A., S. Barba and S. Santini (2005). Normal-fault stress and displacement through finite-element analysis, *Annals of Geophysics*, 48 (6), 1009-1016.
- Melosh, H.J. and A. Raefsky (1981). A simple and efficient method for introducing faults into finite elements computations, *B. Seismol. Soc. Am.*, 71, 1391-1400.
- Meltzner, A.J., K. Sieh, M. Abrams, D.C. Agnew, K.W. Hudnut, J.-P. Avouac, and D.H. Natawidjaja (2006). Uplift and subsidence associated with the great Aceh–Andaman earthquake of 2004, *J. Geophys. Res.*, 111, B02407; doi: 10.1029/2005JB003891.
- Mooney, W.D., G. Laske and G. Masters (1998). CRUST 5.1: A global crustal model at  $5^\circ \times 5^\circ$ , *J. Geophys. Res.*, 103 (B1), 727-747.
- Nostro, C., A. Piersanti, A. Antonioli and G. Spada (1999). Spherical versus flat models of coseismic and postseismic deformations, *J. Geophys. Res.*, 104, 13115-13134.
- Okada, Y., 1985. Surface deformation due to shear and tensile faults in a half-space, *B. Seismol. Soc. Am.*, 75, 1135-1154.
- Okada, Y., 1992. Internal deformation due to shear and tensile faults in a half-space, *B. Seismol. Soc. Am.*, 82, 1018-1040.
- Park, J., T.-R.A. Song, J. Tromp, E. Okal, S. Stein, G. Roullet, E. Clevede, G. Laske, H. Kanamori, P. Davis, J. Berger, C. Braitenberg, M. Van Camp, X. Lei, H. Sun, H. Xu and S. Rosat (2005). Earth's Free Oscillations Excited by the 26 December 2004 Sumatra–Andaman Earthquake, *Science*, 308, 1139-1144.
- Piersanti, A., G. Spada and R. Sabadini (1997). Global post-seismic rebound of a viscoelastic Earth: Theory for finite faults and applications to the 1964 Alaska earthquake, *J. Geophys. Res.*, 102, 477-492.
- Stein, S. and E. Okal (2005). Speed and Size of the Sumatra Earthquake, *Nature*, 434, 581-582.
- Subarya, C., M. Chlieh, L. Prawirodirdjo, J.-P. Avouac, Y. Bock, K. Sieh, A.J. Meltzner, D.H. Natawidjaja and R. McCaffrey (2006). Plate-boundary Deformation of the Great Aceh–Andaman Earthquake, *Nature*, 440; doi: 10.1038/nature04522.
- Tobita, M., H. Suito, T. Imakiire, M. Kato, S. Fujiwara and M. Murakami (2006). Outline of vertical displacement of the 2004 and 2005 Sumatra earthquakes revealed by satellite radar imagery, *Earth Planets Space*, 58, e1-e4.
- Tsai, V.C., M. Nettles, G. Ekström and A.M. Dziewonsky (2005). Multiple CMT source analysis of the 2004 Sumatra earthquake, *Geophys. Res. Lett.*, 32, L17304.
- Vallée, M. (2007). Rupture properties of the giant Sumatra earthquake imaged by empirical Green function analysis, *B. Seismol. Soc. Am.*, 97 (1A), S103-S114.
- Vigny, C., W.J.F. Simons, S. Abu, R. Bamphenyu, C. Satirapod, N. Choosakul, C. Subarya, A. Socquet, K. Omar, H.Z. Abidin and B.A.C. Ambrosius (2005). Insight into the 2004 Sumatra–Andaman earthquake from GPS measurements in southeast Asia, *Nature*, 436, 201-206.
- Volpe, M., D. Melini and A. Piersanti (2007). FEMSA: A finite element simulation tool for quasi-static deformation modeling, *Annals of Geophysics*, 50 (3), 367-385.
- Xing, H.L. and A. Makinouchi (2000). A node-to-point contact

element strategy and its applications, RIKEN Rev.: High Performance Computing, 30, 35-39.

Xing, H.L. and A. Makinouchi (2002). Finite element modeling of multi-body contact and its application to active faults, Concurrency and Computation: Practice and Experience, 14, 431-450.

---

\*Corresponding author: Manuela Volpe,  
Istituto Nazionale di Geofisica e Vulcanologia – INGV, Rome, Italy;  
email: manuela.volpe@ingv.it.

© 2011 by the Istituto Nazionale di Geofisica e Vulcanologia. All rights reserved.